ACS OMEGA

http://pubs.acs.org/journal/acsodf
Article

Facile Synthesis of Multifunctional Carbon Dots Derived from Camel Milk for Mn^{7+} Sensing and Antiamyloid and Anticancer Activities

Rahul Kumar, Antony Vincy, Khushboo Rani, Neha Jain, Sarvar Singh, Ajay Agarwal, and Raviraj Vankayala*

Cite This: *ACS Omega* 2023, 8, 36521−36533
Read Online

ABSTRACT: Carbon dots (CDs) are promising biocompatible fluorescent nanoparticles mainly used in bioimaging, drug delivery, sensing, therapeutics, and various other applications. The utilization of natural sources and green synthetic approaches is resulting in highly biocompatible and nontoxic nanoparticles. Herein, we report an unprecedented facile and green synthesis of highly luminescent carbon dots derived from camel milk (CM) for sensing manganese (Mn^{7+}) ions and for identifying the anticancer potential and antiamyloid activity against α-synuclein amyloids. α-Synuclein amyloid formation due to protein misfolding (genetic and environmental factors) has gained significant attention due to its association with Parkinson's disease and other synucleinopathies. The as-synthesized CM-CDs possess an average hydrodynamic diameter ranging from 3 to 15 nm and also exhibit strong photoluminescence (PL) emission in the blue region. The CM-CDs possess good water dispersibility, stable fluorescence under different physical states, and outstanding photostability. Moreover, the CM-CDs are validated as an efficient sensor for the detection of Mn^{7+} ions in DI water and in metal ion-polluted tap water. In addition, the CM-CDs have demonstrated a very good quantum yield (QY) of 24.6% and a limit of detection (LOD) of 0.58 μM for Mn^{7+} ions with no incubation time. Consequently, the exceptional properties of CM-CDs make them highly suitable for a diverse array of biomedical applications.

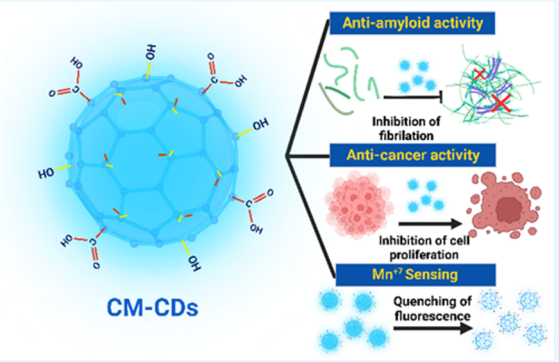

1. INTRODUCTION

In recent years, nanomaterials have been widely explored for various applications, including chemical industries, optics, electronics, sensors, and pharmaceuticals.[1,2] It mostly includes zero-dimensional (dots, nanoparticles), one-dimensional (nanowires, nanotubes), two-dimensional (nanosheets), and three-dimensional (polycrystal) particles having distinct sizes and morphologies. The use of natural sources as precursors in nanomaterial synthesis enables a robust, facile, green, and cost-effective fabrication of potentially nontoxic nanostructures.[3,4] To this end, plant extracts and naturally available materials were used as precursors.[5−7] Furthermore, the utilization of specific precursors, namely, ginger, date pits, ibuprofen, and *β vulgaris*, has been demonstrated to yield nanostructures possessing distinct medicinal properties. Given the advantage that carbon dots can be fabricated using any natural source, herein, we have developed an unprecedented facile and green synthesis of highly luminescent carbon dots derived from camel milk (CM). CM is an emulsion of butterfat globules, closest to human milk in terms of nutritional content.[8,9] CM is consumed regularly as a food source, and it has already been considered to have medicinal characteristics.[10] It comprises low sugar, low cholesterol, and high minerals like sodium, potassium, iron, copper, zinc, magnesium, and vitamin C.[11−14] CM and its products are well explored for various health benefits in cancer, Parkinson's disease, and diabetes and have antihypersensitive activity.[15−17]

The abundance of medium-chain fatty acids, lactose, and other bioactive compounds makes it excessively rich in carbon compared to other milk sources.[9,18] The use of CM in the synthesis of carbon dots (CM-CDs) for various biomedical applications offers an extra advantage to its utilization in the biomedical field. Owing to its unique photoluminescence (PL) properties, CDs have attained remarkable attention for a wide range of biomedical applications.[18] Moreover, they also possess excellent physical and chemical properties, including good aqueous solubility, flexibility for functionalization, inertness, biocompatibility, optical stability, and low toxicity.[19−21] Fluorescent CDs have been employed in various applications such as photocatalysis, cellular imaging, diagnostics, therapeutics, sensors and biosensors, and as a selective probe for

Received: July 27, 2023
Accepted: September 5, 2023
Published: September 20, 2023

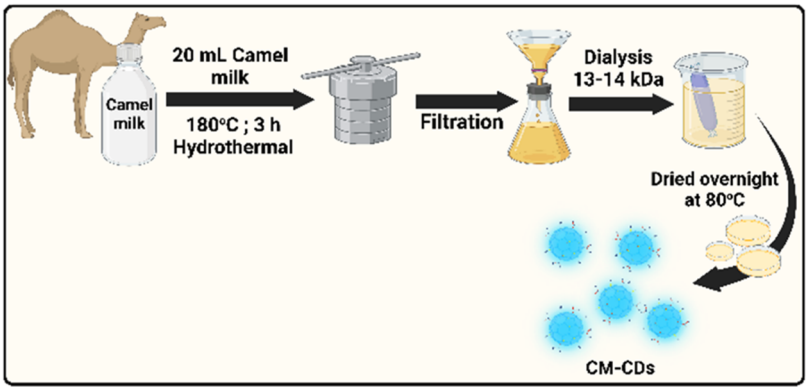

Figure 1. Schematic representation of the synthesis of CM-CDs derived from camel milk. The artwork is created using licensed BioRender software.

detecting organic and inorganic molecules.[21−24] In particular, for sensing applications, CDs have been reported to be very sensitive and selective for the detection of metal ions, which play an important role in the environmental pollution and regulation of certain activities in biological systems.[25−28]

Heavy metal ions such as Pd^{2+}, Hg^{2+}, Fe^{2+}, Cu^{2+}, Mn^{7+}, Cr^{6+}, etc., have posed a serious hazardous effect on the surrounding environment and human health.[29] It has been reported that in India, 40% of industrial waste is dumped untreated into water bodies and in open lands.[30] Manganese is one such essential heavy metal ion required for metabolism, brain functioning, enzyme activity, antioxidant system, and many physiological processes.[31] Though it is essential, its excessive intake leads to hallucination, madness, gene mutation, and a condition called manganism, which is a neurodegenerative disease having symptoms like Parkinson's disease and dopaminergic neuronal disease.[32−34] Excessive intake of Mn leads to an increased risk of Parkinson's disease (PD).[35] A recent study by Bingkuan Xu et al. showed that Mn can act as an environmental risk factor for PD, where it promotes α-synuclein phase transition (soluble liquid α-synuclein monomers to solidlike condensates) and facilitates amyloid assembly.[35] PD is one of the most common and the world's fastest growing neurodegenerative disease characterized by the accumulation of α-synuclein amyloid fibrils as Lewy bodies inside the cell body of the neuron.[36] The presence of amyloids results in the degeneration of dopaminergic neurons in the substantia nigra of the midbrain leading to motor symptoms like rigidity, tremor, and bradykinesia and nonmotor symptoms like depression, anxiety, and sleep disorders in Parkinson's disease patients.[37] The exact reason for the initiation of α-synuclein amyloid fibril formation still remains to be deciphered.

Several environmental toxins such as metal ions, along with genetic mutations and post-translational modifications associated with α-synuclein, contribute to α-synuclein amyloid formation.[38] α-Synuclein (α-Syn), a cytoplasmic intrinsically disordered protein, is located in the presynaptic neuron in the brain.[39] Although its physiological function is not yet known, it is believed to be involved in the release of neurotransmitters, vesicle trafficking, and clustering and maintenance of the SNARE protein complex.[40,41] The C-terminal region of α-syn contains multiple Asp and Glu residues, which interact with many divalent and trivalent metal ions. Among these metal ions, Mn is an essential metal ion involved in many physiological processes and can be found in several oxidation states: +2, +3, +4, +6, and +7.[42] Among all of these, Mn^{2+} and Mn^{7+} are most prominent. While Mn^{2+} is the most stable oxidation state of Mn in natural water and also gets concentrated in the brain and binds to α-syn,[43] Mn^{7+} is a very strong oxidant used in chemical industries, and it is considered hazardous to human health by virtue of its stability and carcinogenic characteristics.[31,44] Food and industrial pollutants are the major sources of Mn^{7+} contamination. Conventional Mn^{7+} detection methods like solid phase extraction (SPE), flame atomic absorption spectrometry (FAAS), and graphite furnace atomic absorption spectrometry need highly specialized instruments and complicated procedures that take more time and are expensive.[45] Alternative detection strategies utilizing fluorophores such as CDs, quantum dots, organic dyes, nanoparticles, and others have been investigated to address the limitations associated with conventional methods as they are simple, sensitive, rapid, and affordable.[23,46−48] Several reports employ CDs for the selective and sensitive fluorescence-based detection of Mn^{7+}. However, the synthesis involves reagents like acids and nitrates, which makes the procedure environmentally toxic and expensive.[49−53]

In this study, for the first time, we have demonstrated the synthesis of highly luminescent CDs derived from CM using a completely green hydrothermal approach (Figure 1).[54] To the best of our knowledge, CM has never been explored in the synthesis of any nanoparticles (including CDs) for sensing and/or any other biomedical applications, such as antiamyloid and anticancer activities. As a matter of fact, milk from any source can be utilized for the synthesis of carbon dots, albeit camel milk makes it superior in terms of its potential medicinal benefits.

2. MATERIALS AND METHODS

2.1. Materials. CM was bought from a local milk vendor in Jodhpur, Rajasthan. Poly(vinylidene fluoride) (PVDF) syringe filters (0.11 μm (SF7) and 0.22 μm (SF10)) and a dialysis membrane 70 (LA393-5MT) were purchased from HiMedia Laboratories Pvt. Ltd., Mumbai, India. Whatman filter papers (1441-125) of 125 mm size were procured from Global Life Solutions Pvt. Ltd., India. Potassium permanganate ($KMnO_4$, 25100), calcium nitrate ($Ca(NO_3)_2$, 22490), cobalt chloride ($CoCl_2$, 22590), nickel nitrate ($Ni(NO_3)_2$, 24390), and gadolinium(III) nitrate hexahydrate ($GdH_{12}N_3O_{15}$, 211591) were purchased from MolyChem Chemicals, India. Magnesium nitrate ($Mg(NO_3)_2$, Q25175) was purchased from Qualigens Pharma Pvt. Ltd., India. Manganese(II) chloride

https://doi.org/10.1021/acsomega.3c05485
ACS Omega 2023, 8, 36521−36533

solutions ($MnCl_2$, 48795), lead(II) acetate trihydrate ($Pb(C_2H_3O_2)_{2.3}(H_2O)$, 467863), cadmium acetate dihydrate ($C_2H_6CdO_3$, 289159), copper(II) acetate ($Cu(CH_3COO)$, 326755), zinc chloride ($ZnCl_2$, Z4875), mercury(II) acetate ($C_4H_6O_4Hg$, 83352), and dimethyl sulfoxide (DMSO, 20-139) were purchased from Sigma-Aldrich Chemicals Pvt. Ltd., India. 3-(4,5-Dimethylthiazol-2-yl)-2,5-diphenyl-2H-tetrazolium bromide (MTT) reagent was purchased from Invitrogen BioServices India Pvt. Ltd., India. All other reagents used for experiments were of analytical grades and were used without further purification.

2.2. Cell Culture. NIH/3T3 (mouse fibroblasts), A549 (lung adenocarcinoma, human), and SHSY59 (neuroblastoma, human) cells were purchased from the National Centre for Cell Science (NCCS), India and cultured in high glucose Dulbecco's modified Eagle's medium (DMEM, Sigma-Aldrich Chemicals) at 37 °C and under a 5% CO_2-enriched atmosphere.

2.3. Preparation of CM-CDs. For the synthesis, 25 mL of CM and 20 mL of deionized (DI) water were mixed in a beaker under vigorous stirring. The mixture was added to a Teflon container and hydrothermally processed at 180 °C for 3 h in a hot air oven. Once cooled, the carbonized solution was filtered through a Whatman filter paper (125 mm) and then filtered through 0.22 μm PVDF syringe filters. The particles were then first dialyzed through a 12−14 kDa membrane and dried at 80 °C. The stock solutions were prepared from dried CM-CDs, sonicated, and passed through 0.22 and 0.11 μm syringe filters sequentially for further experiments.

2.4. Instrumentation. A KL-103 hot air universal oven was used for the hydrothermal process. It is equipped with an i-therm (AI-7982) temperature controller. UV absorption spectra were recorded on a UV-1900i (Shimadzu) spectrophotometer. Fluorescence measurements were carried out on an FP-8300 (Jasco) spectrofluorometer. It comprises a continuous output Xe arc lamp as the broadband light source. A UV flashlight (LUMENSHOOTER) 365 nm, high power 18650 LED torch was used to irradiate the test samples. Fourier transform infrared (FT-IR) spectral measurements were carried out using an LS55 (PerkinElmer) FT-IR spectrometer. X-ray photoelectron spectroscopy (XPS, Scienta Omicron) was used for XPS measurements. Specac's manual hydraulic press (AZO materials) was used to prepare a KBr pellet. Powder X-ray diffraction (XRD) patterns were recorded on a Shimadzu XRD-6000 diffractometer with Cu Ka radiation. The solution pH values were measured with an LMPH-10 pH meter (LABMAN Scientific Instruments). Raman spectral measurements were carried out using a Nomadic multiwave Raman microscope V4.0.0.1 (BAY SPEC) with an integrated 532 nm laser (30 mV) and motorized ND filters. The size of the CM-CDs was analyzed under a JEOL-2100 transmission electron microscope (TEM) at 200 kV. The height profile of the CM-CDs was obtained through an XE 70 Advance scanning probe microscope (Park Systems). The size and zeta potential measurements were carried out on a Malvern Analytical Zetasizer Ultra (Malvern Panalytical) system. It uses multi-angle dynamic light scattering (MADLS) for size measurements and electrophoretic light scattering (ELS) with M3-PALS and a constant current zeta mode for zeta potential measurements.

2.5. Preparation of Stock Solutions. The CM-CDs stock solutions were prepared in deionized (DI) water and stored at 4 °C. Metal ion stock solutions (10 mM) were freshly prepared in DI water and further used for sensing experiments, according to the desired concentration. Real-time samples for Mn^{7+} sensing were prepared by spiking the respective metal ions into tap water. MTT stock solutions were prepared in phosphate-buffered saline (PBS) solution.

2.6. UV−vis and Fluorescence Spectroscopy. The UV absorption spectra for the CM-CDs were recorded from the 250−600 nm wavelength region with a fixed slit width of 1 nm. DI water was used as the baseline, and the scanning speed was kept medium for all of the measurements. The fluorescence spectra for the CM-CDs were recorded in the wavelength ranging from 295 to 600 nm. A slit width of 5 nm was used for excitation and that of 10 nm was used for emission, respectively. The dried CM-CDs were diluted to 10 $\mu g\ mL^{-1}$, sonicated, and filtered through 0.22 and 0.11 μm syringe filters sequentially to characterize PL properties. Visual fluorescence was analyzed under a UV flashlight and quantified using a fluorescence spectrophotometer. The fluorescence spectra of the CM-CDs were recorded for a range of excitation wavelengths from 280 to 600 nm to know the excitation-dependent emission behavior. They were mapped in an excitation−emission matrix (EEM) from 280 to 600 nm. The CM was also tested under identical conditions as a control to prove the PL emission of CM-CDs.

2.7. AFM, DLS, and Zeta Potential Measurements. The morphology of the CM-CDs was examined through dynamic light scattering (DLS) and atomic force microscopy (AFM) measurements. The surface charge of the CM-CDs was examined through zeta measurements. A low-volume quartz batch cuvette (ZEN2112) and a disposable folded capillary cell (DTS1070) were used for DLS and zeta measurements. A 10 $\mu g\ mL^{-1}$ sample was used for both DLS and zeta measurements.

2.8. Interaction of Metal Ions with CM-CDs; Mn^{7+} Sensing. The CM-CDs were tested for their selectivity and sensing capability with regard to various metal ions. Some metal ions (cations), i.e., Ni^{2+}, Cu^{2+}, Ca^{2+}, Mg^{2+}, Mn^{7+}, Mn^{2+}, Gd^{3+}, Pd^{2+}, Cd^{2+}, Cu^{2+}, Zn^{2+}, and Hg^{2+} at 500 μM concentration were incubated with 10 $\mu g\ mL^{-1}$ CM-CDs solution and tested for fluorescence quenching. The fluorescence spectra were recorded at 320 nm photoexcitation immediately after incubation with all different metal ions. The integrated fluorescence intensity was quantified to determine the selectivity and sensitivity toward Mn^{7+} ions. From all of the tested metal ions, Mn^{7+} ions showed almost complete quenching. Further, only Mn^{7+} ions were tested for fluorescence quenching, ranging from 0 to 500 μM at similar conditions and parameters. The CM-CDs showed very good linearity in fluorescence quenching from 0 to 100 μM. Then, the correlation of the quenching efficiency with the concentration of metal ions was plotted to analyze the LOD for the CM-CDs. All experiments related to sensitivity and selectivity were carried out in triplicate and at room temperature.

2.9. Quantum Yield Measurements. The QY of CM-CDs was obtained by choosing quinine sulfate as the reference dye. The UV−vis absorption spectrum was taken for five different concentrations, with the absorbance value kept below 0.1. The PL emission spectra were measured for the same concentrations with a 320 nm excitation wavelength. Then, the QY (%) was calculated from the following equation

https://doi.org/10.1021/acsomega.3c05485
ACS Omega 2023, 8, 36521−36533

$$\emptyset_x = \emptyset_s * \left(\frac{m_x}{m_s}\right)\left(\frac{\eta_x^2}{\eta_s^2}\right) \quad (1)$$

Here, Ø is the QY and x and s are referred to as the CM-CDs sample and reference, respectively. m is the slope of the calibration curve for the integrated fluorescence intensity of both samples calculated from the PL spectra for the defined concentrations. η is the refractive index of the solvent used, which is 1.33 for both reference and sample CM-CDs. Then, the QY is calculated as

$$\text{then QY is calculated as: } \mathrm{QY}(\%) = \left(\frac{\emptyset_x}{\emptyset_s}\right) \times 100 \quad (2)$$

2.10. Mn^{7+} Sensing in Real-Time Samples. The CM-CDs were tested for their selectivity in mixed metal ion-polluted tap water samples. To make the real-time test sample, all of the metal ions such as Ni^{2+}, Cu^{2+}, Ca^{2+}, Mg^{2+}, Mn^{2+}, Gd^{3+}, Pd^{2+}, Cd^{2+}, Cu^{2+}, Zn^{2+}, and Hg^{2+} at 100 μM and 500 μM concentrations were mixed in 10 μg mL^{-1} CM-CDs solution in tap water. Mn^{7+} ions were sensed in the presence of all other metal ions under each condition. Here, a 10 μg mL^{-1} CM-CDs solution in tap water was taken as a negative control. The fluorescence spectra were recorded at 320 nm immediately after incubation with Mn^{7+} ions at different concentrations. The integrated fluorescence intensities were quantified and plotted against Mn^{7+} ions to determine the selectivity toward Mn^{7+} ions. Visual detection for Mn^{7+} ions was enabled using a UV flashlight. Glass vials and solid dipstick sensors were used to demonstrate the visual detection of Mn^{7+} sensing in a polluted tap water sample. Solid dipstick sensors were fabricated using CM-CDs (10 μg mL^{-1}) and agar (1%) solutions over glass slides.

2.11. PL Stability of CM-CDs at Different pH, Temperature, and under Light Irradiation. The fluorescence stability of the CM-CDs at different temperatures (4 and 37 °C), pH (pH 1−11), and under light irradiation was studied. The fluorescence spectra were taken, and the integrated fluorescence intensity was quantified for all of the stability experiments. Photostability was quantified using both absorption and fluorescence measurements. For temperature stability, 10 μg mL^{-1} CM-CDs solution in DI water was kept at 4 and 37 °C for 14 days, and the fluorescence spectra were taken on every alternate day. For pH stability experiments, a 10 μg mL^{-1} CM-CDs solution was prepared in different pH solutions, and the PL spectra were recorded. For photostability, 10 μg mL^{-1} CM-CDs were irradiated using a halogen lamp for a continuous 2 h. The fluorescence spectra were taken at different time points for 2 h, and absorbance was measured using a FLUOstar Omega plate reader spectrophotometer (BMG LABTECH, Germany) at a 320 nm excitation wavelength. All of the experiments related to stability were carried out in triplicate.

2.12. Expression and Purification of α-Synuclein (α-Syn). A standard protocol for α-syn purification was followed as mentioned in the litreature.[55] Briefly, the α-syn gene was expressed in the pT7-7 plasmid and transformed into BL21 (DE3) cells for overexpression and purification. A single colony was inoculated in LB media containing 100 μg mL^{-1} ampicillin and incubated overnight at 37 °C at 200 rpm. The overnight culture was inoculated in fresh LB media until an O.D. 0.6 at 600 nm and induced with 0.8 mM IPTG for 4 h. The induced culture was pelleted down at 4000 rpm for 20 min at 4 °C. The obtained pellets were lysed in lysis buffer (50 mM Tris, 150 mM NaCl, 10 mM EDTA, pH 8), heated at 95 °C for 30 min, and centrifuged at 12,000 rpm for 30 min at 4 °C. The supernatant was collected and mixed with 10% streptomycin sulfate (136 μg mL^{-1}) and glacial acetic acid (228 μL). An equal volume of saturated ammonium sulfate was added for protein precipitation and kept at 4 °C with intermittent mixing for 1 h and centrifuged. To wash the protein pellet, an equal amount of 100 mM ammonium acetate and absolute ethanol was added, and then the pellet was finally washed with absolute ethanol two times. The obtained pellets were dried at RT and resuspended in 50 mM potassium phosphate buffer (pH 7.4) and stored at −80 °C. Before every experiment, a 0.1 μm filter was used to filter the protein, and the purity was confirmed on SDS-PAGE.

2.13. α-Syn Aggregation Kinetics and Spectral Measurement. An α-syn aggregation reaction was performed in a flat black 96-well plate (Corning, Thermo Fisher Scientific) using a FLUOstar Omega plate reader spectrophotometer (BMG LABTECH, Germany). The 100 μL of total reaction volume consisted of 100 μM α-syn, 100 mM NaCl, and 20 μM ThT in 50 mM potassium phosphate buffer (pH 7.4) with a 2 mm glass bead, and the plate was sealed with an optical sealer to avoid evaporation. The reaction was carried out at 200 rpm with continuous shaking at 37 °C without and with CM-CDs. The fluorescence intensity was measured at every 1 h interval in the double orbital shaking mode with an excitation filter of 440 nm and an emission filter of 490 nm.[55] To check the effect of CM-CDs, the reaction was performed under similar conditions in the presence of 3 mg mL^{-1} CM-CDs. The ThT spectra were taken before and after the reaction sample using a FP-8300 fluorescence spectrometer (JASCO Japan). The samples were excited at 440 nm and the spectra were recorded from 460 to 600 nm using a 1 mm path length cuvette. Excitation and emission slits were used at 2.5 and 5 nm, respectively. Each spectrum was an average of two scans with a 100 nm/min scan speed at RT.

2.14. Fluorescence Microscopy. α-Syn without and with CM-CDs and only CM-CDs were aliquots from the ThT kinetic reaction at 0 and 30 h. The samples were drop-casted on a clean glass slide, covered with a coverslip, and visualized in a FLoid cell imaging station (Thermo Fisher Scientific) using a FITC filter (Ex. wavelength 482/18 nm and Em. wavelength 532/59 nm).[56]

2.15. Field Emission Scanning Electron Microscopy (FE-SEM). Ten μL of α-syn without and with CDs after 30 h of ThT kinetic reaction was adsorbed on a silica wafer and incubated for 2−3 min. The samples were washed 3 times with 100 μL of 0.1 μ filter milli-Q water and dried overnight in a vacuum desiccator. On the next day, the samples were sputter-coated with gold for 60 s and imaged using an OptiPlan detector at 1,20,000× magnification and an accelerating voltage of 5 kV in a field emission scanning electron microscope (Apreo 2S from Thermo Fisher Scientific).[57]

2.16. Circular Dichroism (CD) Spectroscopy. The far-UV CD spectra of the ThT kinetic reaction samples were recorded before and after the reaction using a JASCO-815 CD spectrophotometer (JASCO, Japan). Twenty μM α-syn in 50 mM potassium phosphate buffer (pH 7.4) was used to record the CD spectra from 195 to 250 nm with a scan speed of 100 nm/min using a quartz cuvette with 1 mm path length. Each spectrum was an average of two scans.[58]

https://doi.org/10.1021/acsomega.3c05485
ACS Omega 2023, 8, 36521−36533

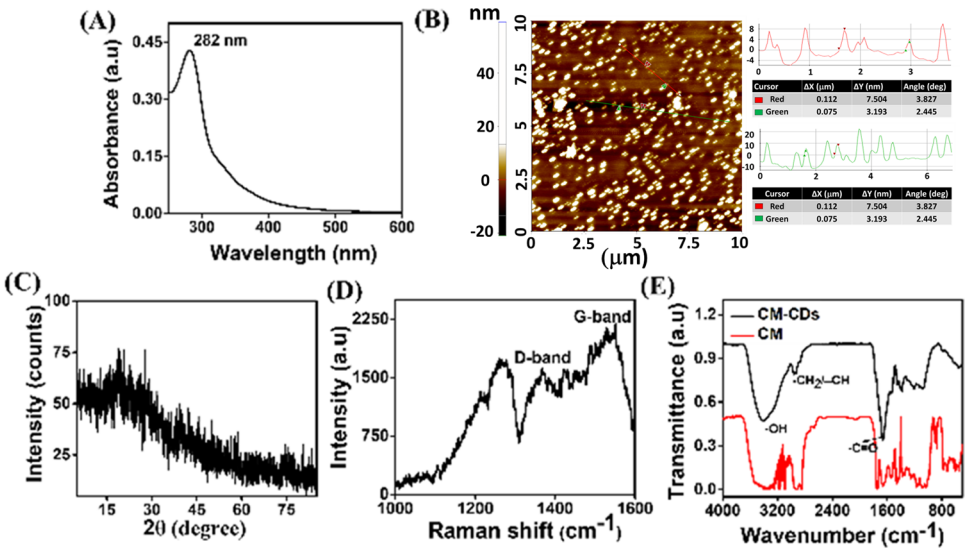

Figure 2. Characterization of CM-CDs. (A) UV−vis absorption spectra, (B) AFM image and height profile of CM-CDs, (C) XRD spectra for CM-CDs, (D) Raman spectrum for CM-CDs, and (E) FT-IR spectrum for CM-CDs and CM.

2.17. Cell Cytotoxicity Assay (MTT). The cytotoxicity of the CM-CDs was studied to examine biocompatibility and the inherent anticancer property of the material. The MTT assay was utilized to determine the viability of NIH/3T3, A549, and SHSY59 cells. For that, 8000 cells per well were inoculated in a 96-well plate (TARSONs) with 200 mL of DMEM. After 24 h of spreading, the cells were treated with CM-CDs at concentrations ranging from 10 to 250 mg mL^{-1} and incubated at 37 °C for 24 h in a humidified incubator containing 5% CO_2. After 24 h of treatment with CM-CDs, 10 mL of an MTT solution (5 mg mL^{-1}) was added to each well. After 4 h of incubation, the MTT solution was carefully removed and 100 mL of DMSO was added to dissolve the formazan crystals (viable cells exhibit a notable increase in absorbance values in comparison to nonviable cells due to the production of abundant purple formazan crystals through the reduction of MTT within their mitochondria). At 570 nm, absorbance was measured with a FLUOstar Omega plate reader spectrophotometer. Cell viability (%) was calculated from the relationship of absorbance, i.e., $(A_{sample}/A_{control}) \times 100$. Each concentration was tested three times, and every experiment was conducted in duplicate for this assay.

2.18. Hemolysis Assay. The hemolysis assay was conducted in accordance with previously established protocols.[59] Fresh blood was collected from AIIMS, Jodhpur. Red blood cells (RBCs) were isolated through centrifugation of the blood sample (1 mL) at 1500 rpm for 10 min. The liquid portion comprising plasma and platelets were discarded. The RBCs were washed three more times with PBS. Then, the pellet of RBCs was reconstituted in 3 mL of PBS. Subsequently, a volume of 0.1 mL of the RBC suspension that had been diluted was introduced to a mixture of 0.9 mL of CM-CDs at varied concentrations. All of the concentrations were taken in triplicate. The resulting suspension was then stored under static conditions at 37 °C for a duration of 4 h. Subsequently, the samples were centrifuged at 15,000 rpm for 10 min to sediment the RBCs. The optical density of the supernatant was measured at a wavelength of 575 nm, corresponding to the absorbance of hemoglobin. The negative and positive controls were prepared using a diluted RBC suspension of 0.1 mL, which was incubated with 0.9 mL of PBS and 0.9 mL of deionized water, respectively. The percentage of hemolysis was computed using the following formula:

$$\text{hemolysis}(\%) = \frac{((\text{O.D})_{\text{sample}} - (\text{O.D})_{\text{negativecontrol}})}{(\text{O.D})_{\text{positivecontrol}} - (\text{O.D})_{\text{negativecontrol}}} \quad (3)$$

3. RESULTS AND DISCUSSION

3.1. Characterization of CM-CDs. The CM-derived CDs were prepared using a hydrothermal approach. The as-synthesized CM-CDs were characterized by using various spectroscopic and microscopic techniques. Figure 2(A) represents the UV−vis absorption spectra of CM-CDs synthesized by using CM as a carbon source. The UV−vis absorption spectra of the CM-CDs showed strong absorption in the UV region, exhibiting a peak at a wavelength of 282 nm. This is presumably due to the $\pi-\pi^*$ transition of the C═C bonds in the CDs.[60] The particle size distribution of CM-CDs was analyzed by DLS and maximum particles were found to be 3−15 nm with a PDI value of 0.3 (Figure S1(A)). DLS measurements indicated the homogeneous population of CM-CDs in water, as a PDI of 0.3 and below is considered to be moderately polydispersed in nature.[61] The TEM image of the CM-CDs also revealed the particle size to be <10 nm, which correlates with the DLS measurements (Figure S1(B)). AFM analysis confirmed the height distribution profile, as shown in Figure 2(B).

The XRD analysis, as shown in Figure 2(C), confirmed the crystalline nature of CM-CDs, as evidenced by a broad diffraction peak at 21.42° corresponding to the (002) lattice spacing of graphitic carbon. This validates the graphitelike crystalline nature of CM-CDs. Raman analysis is informative for identifying the morphological features of carbon-based materials. The Raman spectra of the CM-CDs confirmed the presence of a graphitic carbon structure with some defects.

As shown in Figure 2(D), the Raman spectra showed D and G bands at 1370 and 1540 cm^{-1}, respectively, due to the presence of out-of-plane vibrations of structural defects and in-plane vibrations of sp^2 bonded carbon atoms in the structure of

https://doi.org/10.1021/acsomega.3c05485
ACS Omega 2023, 8, 36521−36533

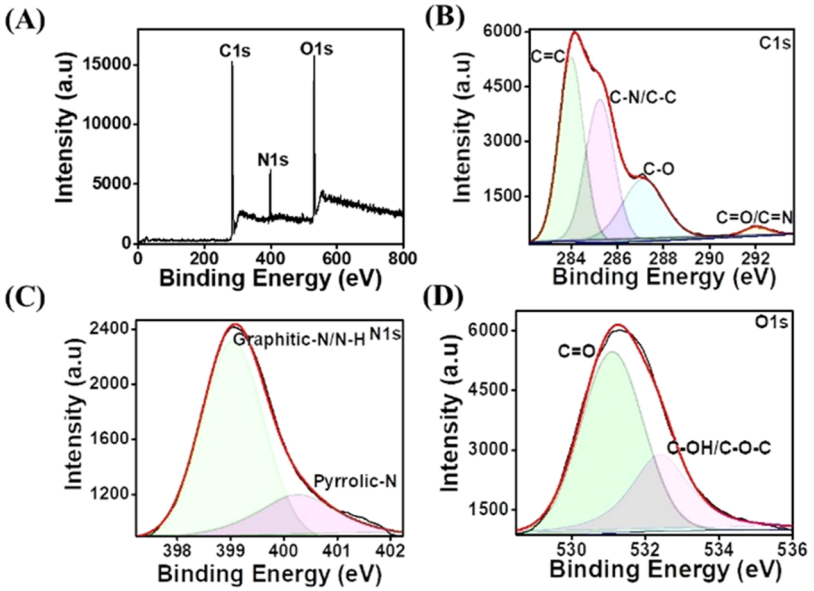

Figure 3. XPS characterizations. (A) Survey scan for CM-CDs. (B–D) High-resolution C 1s, N 1s, and O 1s peaks of the CM-CDs, respectively.

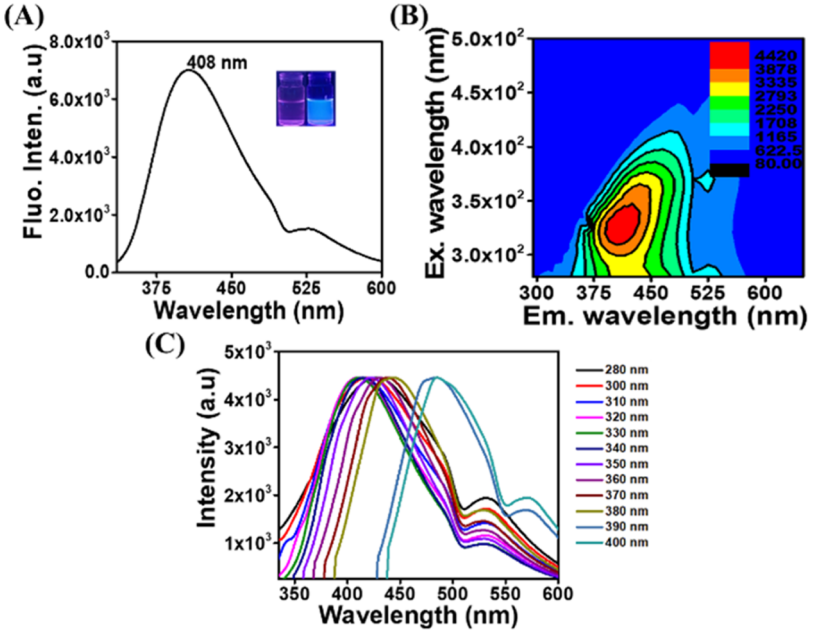

Figure 4. PL properties of CM-CDs. (A) PL emission spectra for CM-CDs. The inset represents the photographs of the blue fluorescence from CDs under a UV illuminator. (B) EEM mapping of CM-CDs. (C) Excitation-wavelength-dependent emission spectra for CM-CDs.

CM-CDs.[62,63] Additionally, the peak at 1272 cm^{-1} corresponded to the presence of amides.[64] FT-IR spectra were recorded for the precursor and CM-CDs to identify the surface functional groups. In Figure 2(E), the FT-IR spectra of CM-CDs exhibited peaks in the 3450–3230, 2937/2868, and 1660 cm^{-1} regions, corresponding to O–H/N–H stretching, C–H stretching vibrations, and amide C=O stretching, respectively. It also suggestsed the presence of O–H and C=O functionalities on its surface, which can impart a net negative charge to CM-CDs.[64] This was further confirmed by the zeta potential measurements of the CM-CDs in DI water. Further, XPS was utilized to investigate the oxidation state and chemical environment of CM-CDs.[65,66] The XPS survey scan revealed distinctive peaks at binding energy levels of 286.12 400.3, and 532.75 eV, corresponding to the C 1s, N 1s, and O 1s orbitals, respectively (Figure 3(A)). The multiplex scan of C 1s exhibited four distinct peaks at 284.05, 285.25, 287.19, and 292 eV, representing the C=C, C–N/C–C, C–O, and C=O/C=N bonds, respectively (Figure 3(B)). The multiplex scan of N 1s displayed peaks at 399.26 and 400.3 eV, corresponding to Free-N/N–H and pyrrolic-N (Figure 3(C)). The multiplex scan of O 1s demonstrated peaks at 531 and 532.38 eV, indicating the presence of C=O and C–OH/C–O–C bonds, respectively (Figure 3(D)). The presence of hydroxyl and carboxyl groups on the surface, as evidenced by various methods, contributes to the water dispersibility of CM-CDs, eliminating the need for additional chemical modifications. The CM-CDs prepared from the hydrothermal process are regarded as rich in amide and hydroxyl groups in the carbonized framework. The observed characteristics of CM-

https://doi.org/10.1021/acsomega.3c05485
ACS Omega 2023, 8, 36521–36533

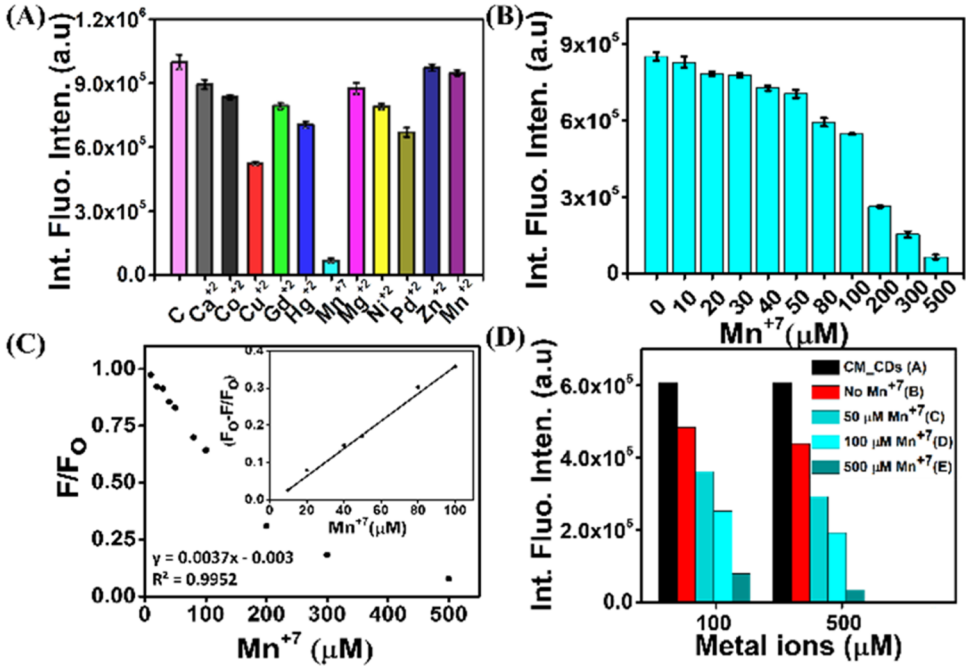

Figure 5. Detection of Mn^{7+} ions. (A) Metal ion sensing with different metal ions at 500 μM concentration (the photoexcitation wavelength is 320 nm). (B) Mn^{7+} sensing using CM-CDs (0−500 mM). (C) Quantification of percent PL quenching with Mn^{7+} ions ranging from 0 to 500 μM and the relationship between quenching efficiency and Mn^{7+} ions (inset). (D) CM-CDs PL quenching in metal ion-polluted samples (0−500 μM).

CDs, including their size, chemical environment, and surface functionalities indicate their potential suitability for various applications.

3.2. PL Properties of the CM-CDs. The as-synthesized CM-CDs exhibited PL in the blue region. As shown in Figure 4(A), the fluorescence emission spectrum of CM-CDs exhibits an emission maximum centered at 408 nm at a photoexcitation wavelength of 320 nm. This further validates the blue emission of CDs under UV illumination.

The EEM mapping of CM-CDs confirms the excitation and emission wavelength hot spots for the brightest PL emission. The strongest emission of CM-CDs is found at an excitation wavelength of 320 nm with an emission maximum at 408 nm (Figure 4(B)). As represented in Figure 4(C), the CM-CDs exhibited an excitation-wavelength-dependent emission when excited in the range of 280−400 nm. The PL emission showed a continuous red shift upon increasing the excitation wavelength. This excitation-wavelength-dependent emission behavior corresponds to the heterogeneous size and different surface-active states of CDs.[67] To validate the PL emission of CM-CDs, bare CM is subjected to PL emission measurements with unchanged parameters. As represented in Figure S2(A), the bare CM has some PL emission in the UV region at lower UV excitation wavelengths, but its effect is nullified at higher UV excitations. Further, it does not illustrate any excitation-wavelength-dependent PL emission behavior like CM-CDs (Figure S2(B)). This further validates that the PL emission is specific to the synthesized CM-CDs. In general, the band gap of the conjugated π-domain in the CD core, emissive traps due to various energy levels of surface chemical groups, and organic fluorophores formed by the carbonization of the small molecule are responsible for the fluorescence of CDs.[68,69]

3.3. Detection of Mn^{7+} Ions. We utilized CM-CDs for sensing Mn^{7+} ions. The maximum detectable fluorescence intensity of CM-CDs was observed at 320 nm excitation at a concentration of 10 μg mL^{-1}. To evaluate the selectivity of CM-CDs toward Mn^{7+} ions, CM-CDs in deionized water were exposed to various metal ions, i.e., Ni^{2+}, Cu^{2+}, Ca^{2+}, Mg^{2+}, Mn^{7+}, Gd^{3+}, Pd^{2+}, Cd^{2+}, Cu^{2+}, Zn^{2+}, and Hg^{2+}, each at a concentration of 500 μM. The main basis for the selective detection of metal ions is the interaction between metal ions and the functional groups of CDs. CDs tend to form complexes when they interact with metal ions, which leads to fluorescence quenching.[24−26] To validate the selectivity, PL emission from 335 to 600 nm was measured at the 320 nm excitation wavelength immediately after incubation with different metal ions. Then, the integrated fluorescence intensity with all different metal ions was plotted together (Figure 5(A)) to observe the selectivity. From all of the metal ions tested, Mn^{7+} showed maximum fluorescence quenching. The fluorescence intensity of the CM-CDs was completely quenched at 500 μM Mn^{7+} ions. Apparently, other metal ions had not shown a significant amount of quenching even when the incubation time was increased to 30 min. This concludes the selectivity for Mn^{7+} ions when compared to the other metal ions at the same concentration. This phenomenon might result from the coordination reaction between the Mn^{7+} ions and the carboxyl and hydroxyl groups present on the surface of the CM-CDs.[70] To evaluate the sensitivity of Mn^{7+} sensing, PL measurements were performed at different concentrations of Mn^{7+} ions, ranging from 10 to 500 μM. Figure 5(B) illustrates the quantitative relationship between the integrated fluorescence intensity of CM-CDs and the concentration of Mn^{7+} ions (the fluorescence traces are shown in Figure S2(C)). The observed fluorescence quenching demonstrated a concentration-dependent behavior, with complete quenching at a Mn^{7+} ion concentration of 500 μM. Having a good linear correlation of quenching efficiency with the concentration of the metal ion proves the efficiency of CM-CDs for efficient detection.[67,71] F is the integrated fluorescence intensity of CM-CDs incubated with metal ions and F_o indicates the integrated fluorescence intensity of the control. In Figure 5(C), F/F_o is

https://doi.org/10.1021/acsomega.3c05485
ACS Omega 2023, 8, 36521−36533

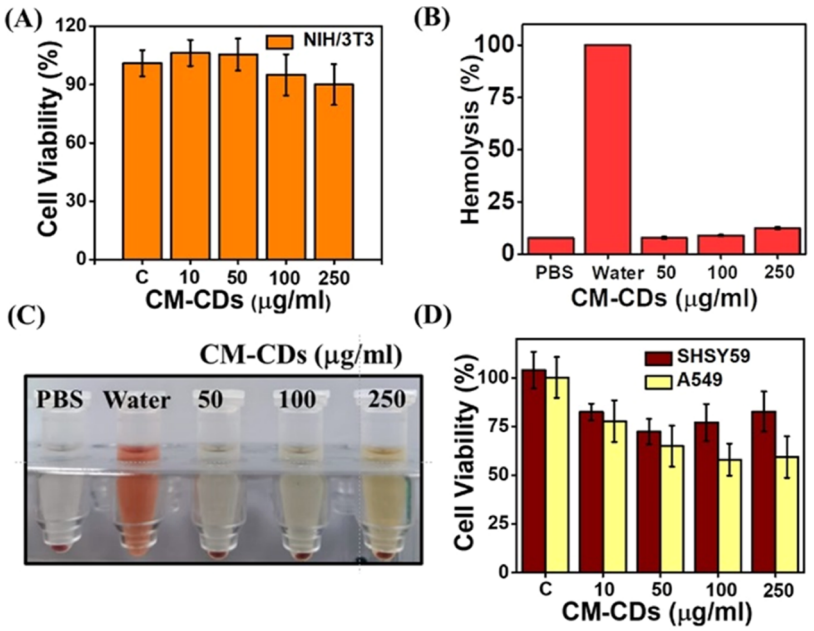

Figure 6. Biocompatibility and anticancer effect of CM-CDs. (A) Cell viability (%) results of NIH/3T3 cell lines with incubation of 24 h with CM-CDs (10−250 mg/mL). (B) Hemolysis (%) results with incubation of 4 h with CM-CDs (50−250 mg/mL). (C) Images representing hemolysis. (D) Cell viability (%) results of SHSY59 and A549 cell lines with incubation of 24 h with CM-CDs (10−250 mg/mL).

plotted against Mn^{7+} ions in DI water from 0 to 500 μM. The integrated fluorescence intensity of CM-CDs in 500 μM Mn^{7+} is found to be less than 10%, which indicates complete quenching by CM-CDs at this concentration. As represented in the inset, there was a very good correlation between the quenching efficiency of CM-CDs and the Mn^{7+} ions in the 0−100 μM range.

This validates the potential use of CM-CDs for the selective and sensitive detection of Mn^{7+} ions in water. The LOD of CM-CDs was calculated using the standard deviation of the response and slope method.[72] The LOD for Mn^{7+} ions was determined to be ∼0.58 μM for the Mn^{7+} ions using CM-CDs as a sensing agent. The CM-CDs were tested for their selectivity in mixed metal ion-polluted tap water samples. To make the real-time test sample, all of the metal ions at 100 and 500 μM concentrations were mixed with the CM-CDs solution in tap water. Each test sample was incubated with three different concentrations of Mn^{7+} ions, i.e., 50 μM (c), 100 μM (d), and 500 μM (e), for the quantification of fluorescence quenching. The PL emission spectra were taken immediately after incubation with Mn^{7+} ions, and the fluorescence intensity was plotted for each concentration for both real-time test samples. The CM-CDs (a) and CM-CDs with metal ion contaminants (no Mn^{7+}(b)) were considered a control for fluorescence quenching comparisons. As represented in Figure. 5(D), the CM-CDs showed excellent selectivity in the presence of metal ion contaminants for both 100 and 500 μM concentrations. The CM-CDs showed little fluorescence quenching in the presence of all metal ion (b) contaminants because of the cationic burden in the solution.[73] This confirms that the CM-CDs have excellent selectivity toward Mn^{7+}, even in the presence of other metal ions. This result validates CM-CDs for Mn^{7+} sensing in industrial pollutants. Our proposed method to sense Mn^{7+} ions using CM-CDs is highly economical and completely green and also offers good selectivity and sensitivity. This study further confirmed the potential of visual detection of Mn^{7+} sensing in real-time tap water-polluted samples (Figure S3). For the fabrication of the solid sensor, the concentration of agar (w/v %) and CM-CDs were optimized (Figure S7). The PL emission of CM-CDs was studied at different physical states like temperature, pH, and under light irradiation. The CM-CDs solution in DI water was incubated at different temperatures (4 and 37 °C) for 14 days, and the PL measurements were taken every alternate day. As shown in Figure S4(A), the integrated fluorescence intensity of CM-CDs remained unchanged for 14 days. The PL emission of CM-CDs at both the temperatures is significantly stable. The CM-CDs solution in DI water was subjected to different pH conditions ranging from 1−11 and incubated for an hour. As shown in Figure S4(B), the integrated fluorescence intensities were found to be slightly high at pH 5, which is not that significant, but it remains almost unchanged for all other pH values. Further, the CM-CDs solution was irradiated using a 300 W halogen lamp for 3 h. It is very clear that the CM-CDs showed excellent photostability and did not undergo any photobleaching (Figure S4(C)).

3.4. Biocompatibility and Anticancer Activity of CM-CDs. The CM-CDs were found to have inherent anticancer properties similar to that of camel milk, with negligible cytotoxicity to normal cells.

In the literature, it was known that the carbon dots prepared from various natural sources such as ginger, date pits, ibuprofen, and *β vulgaris* exhibited anticancer properties similar to that of the precursor.[74] As shown in Figure 6(A), the CM-CDs demonstrated negligible toxicity toward NIH/3T3 cells. The hemolysis experiments reveal that the CM-CDs did not exhibit any significant hemolysis after incubation with red blood cells (Figure 6(B,C)). The absence of hemolysis indicates a lack of red blood cell membrane damage and suggests a high degree of biocompatibility for CM-CDs. However, there is a significant reduction in the cell viability in both A549 and SHSY59 cancer cells upon treatment with CM-CDs for 24 h in a concentration-dependent manner (Figure 6(D)). These findings support that CM-CDs are biocompat-

https://doi.org/10.1021/acsomega.3c05485
ACS Omega 2023, 8, 36521−36533

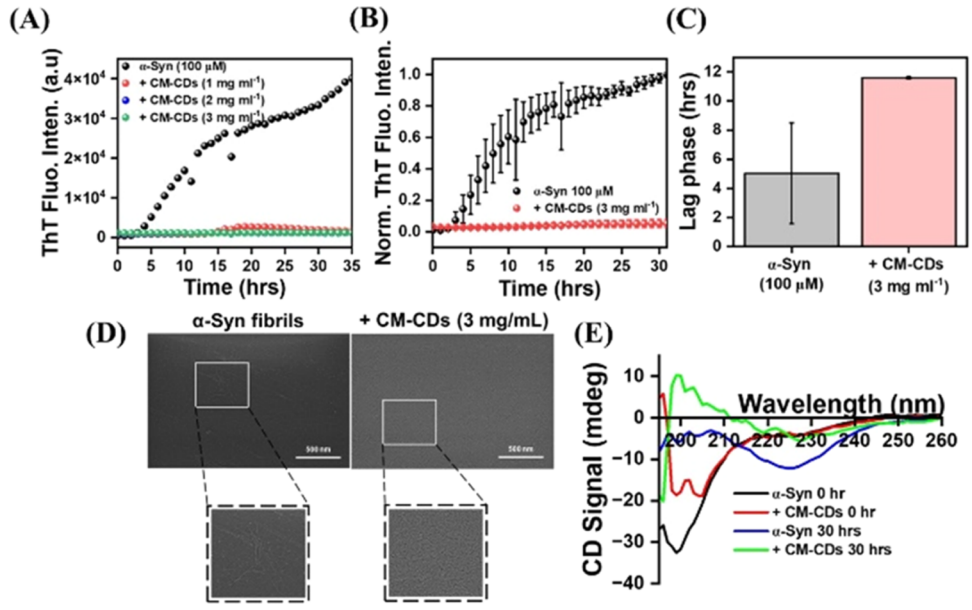

Figure 7. (A) Concentration-dependent inhibition of the α-syn amyloid assembly in the absence and presence of CM-CDs monitored by the ThT fluorescence intensity. (B) Complete inhibition of the α-syn amyloid assembly by 3 mg/mL CM-CDs. (C) Lag-phase deviation of α-syn in the presence or absence of CM-CDs. (D) FE-SEM images and (E) CD spectra in the far-UV region of α-syn fibers without and with CM-CDs at the end of the amyloid assembly.

ible toward normal cells and possess anticancer activity against A549 and SHSY5Y cancerous cells.

3.5. CM-CDs Inhibit α-Synuclein (α-Syn) Amyloid Assembly. To understand the antiamyloid activity of CM-CDs, we monitored the kinetics of the α-syn amyloid assembly using an environmentally sensitive dye, thioflavin T (ThT), which gives strong fluorescence when it interacts with the cross-β sheets of amyloid fibrils.[75] We observed a significant increase in the ThT fluorescence intensity when α-syn was allowed to polymerize alone. The kinetics of α-syn amyloid assembly displayed a sigmoidal curve with a distinguishable lag phase of ~3 h, followed by an exponential phase that attained a stationary phase in 30 h. Upon addition of CM-CDs to α-syn monomers, we observed a concentration-dependent inhibition of the α-syn amyloid assembly (Figure 7(A)). We did not observe any significant increase in ThT fluorescence when 3 mg mL^{-1} CM-CDs were added in 100 μM α-syn, suggesting that CM-CDs completely prevented the α-syn amyloid assembly (Figure 7(B,C)). To overrule the interaction of ThT with CM-CDs, we also performed a control experiment with water, KPi buffer, and CM-CDs under identical aggregation conditions. We did not observe any difference in the ThT fluorescence intensity when incubated with water, KPi buffer, and CM-CDs (Figure S5(A)). The slight increase in the fluorescence of CM-CDs is because of its own PL emission. Specifically, at the ThT excitation wavelength, the CM-CDs also showed some fluorescence, thereby contributing to the overall fluorescence signal observed in the sample. To look further into the microenvironment around ThT, we next recorded the ThT spectra as a function of the evolution of aggregation. No detectable change was observed in the ThT fluorescence intensity in the sample reaction kinetics at 0 h, indicating the presence of ThT in an aqueous environment, where the majority of ThT fluorescence was quenched by the surrounding aqueous medium. However, after 30 h, we observed a significant increase in the ThT fluorescence intensity for α-syn alone, indicating the presence of ThT in a restricted microenvironment of β-sheet-rich amyloids (Figure S5(B)). On the contrary, we did not observe any significant enhancement in the fluorescence intensity when CM-CDs were added to α-syn, suggesting that the CM-CDs suppressed the formation of amyloids and thus ThT fluorescence got quenched in the aqueous environment. The ThT samples at 0 and 30 h were further visualized under a fluorescence microscope. We observed green bloblike structures of α-syn fibrils in 30 h, whereas in the presence of CM-CDs, there was no noticeable green fluorescence (Figure S6(A)).

Further, to strengthen the inhibition of fibrillation, the samples after 30 h were further visualized under a field emission scanning electron microscope (FE-SEM). We observed fibrillar structures of α-syn amyloids in α-syn (Figure 7(D)), whereas in the presence of CM-CDs and in only CM-CDs samples, we failed to notice any fibrillar structure, indicating that the CM-CDs are incapable of transforming α-syn into the amyloid assembly. Next, we investigated the change in the secondary structure of α-syn upon fibrillation in the absence and presence of CM-CDs using far-UV circular dichroism spectroscopy. We observed a transition from a random coil structure to a β-sheet structure when α-syn alone was subjected to amyloid formation. However, α-syn remained mostly in the random coil conformation in the presence of CM-CDs (Figure 7(E)). Our circular dichroism studies further support ThT data that α-syn in the presence of CM-CDs is incapable of transforming into amyloids; rather, it remains in an unstructured soluble form. We also performed a control experiment with 0 and 30 h in water, KPi buffer, and CM-CDs. We did not observe any structural changes in CD spectra under same conditions (Figure S6(B)).

The carbon dots can be easily prepared from any of the natural or synthetic sources. However, among them, the CM-derived CDs will stand out mainly due to the following reasons: (i) green synthesis or chemical-free approach; (ii) excellent PL property; (iii) superior photostability when compared to organic dyes (data not shown); (iv) stability at

https://doi.org/10.1021/acsomega.3c05485
ACS Omega 2023, 8, 36521−36533

physiological and low-temperature conditions; (v) selectivity toward Mn^{7+} ions; (vi) potential to be translated as a dipstick solid sensor (which is useful for industrial applications); (vii) antiamyloid and anticancer properties; (viii) waste-to-useful products (It is known that camel milk has very poor shelf life. The CM-CDs can also be easily prepared from expired camel milk with similar optical properties and sensing capabilities.); and (ix) last but not the least, these CM-CDs also have tremendous potential to exhibit antidiabetic, antibacterial, antihypersensitive, and anti-inflammatory activities, which are very similar to those of camel milk. The CDs prepared from different sources for metal ion sensing have been tabulated (Table S1) for comparison. The CDs prepared from CM have a QY (%) very close to that of the CDs prepared from different sources without any dopant. In addition, CM-CDs are the best among natural resources in terms of the QY (%) and LOD capability. To the best of our knowledge, this is the first demonstration of an unprecedented facile and green synthesis of highly luminescent carbon dots derived from camel milk showing enormous potential for Mn^{7+} sensing applications as well as antiamyloid and anticancer activities. We also foresee that these CM-CDs hold promising prospects for future applications in cancer therapeutics, PD management, and bioimaging fluorescent probes. Further research and development in this field are warranted to explore the full potential of CM-CDs in these areas.

4. CONCLUSIONS

In summary, we report the first demonstration of an unprecedented facile and green synthesis of highly luminescent carbon dots derived from camel milk for sensing manganese ions and for identifying the antiamyloid activity and anticancer potential against α-syn. The as-synthesized CM-CDs possess an average hydrodynamic diameter ranging from 3 to 15 nm and also exhibit strong PL emission in the blue region. The CM-CDs possess good water dispersibility, stable fluorescence under different physical states, and outstanding photostability. The CM-CDs predominantly consist of carboxyl and hydroxyl groups, providing sites for metal ion binding. Moreover, the CM-CDs are validated as an efficient fluorescence sensing agent for detecting Mn^{7+} ions in DI water and in metal ion-polluted tap water. In addition, the CM-CDs have demonstrated a very good QY of ∼24.6% and a LOD value of 0.58 μM for Mn^{7+} ions with no incubation time. The CM-CDs have successfully validated the visual detection of Mn^{7+} sensing under UV irradiation and identified the unique antiamyloid activity against α-syn amyloid assembly in vitro. Apart from sensing, the CM-CDs are found to be biocompatible and also possess anticancer activities similar to those of the precursor (i.e., camel milk). Overall, camel milk-derived carbon dots will have several multifunctionalities, such as for sensing Mn^{7+} ions in industrial effluents and also for various other biomedical applications, which can provide leads for early diagnosis and treatment of amyloidogenic diseases and therapeutic interventions.

■ ASSOCIATED CONTENT

Supporting Information

The Supporting Information is available free of charge at https://pubs.acs.org/doi/10.1021/acsomega.3c05485.

DLS measurements, additional PL emission spectra, visual representation of Mn^{7+} sensing, and some additional data for antiamyloid fibril formation are available in the Supporting Information (PDF)

■ AUTHOR INFORMATION

Corresponding Author

Raviraj Vankayala − *Department of Bioscience and Bioengineering, Indian Institute of Technology Jodhpur, Karwar 342030, India; Interdisciplinary Research Platform Smart Healthcare, Indian Institute of Technology Jodhpur, Karwar 342030, India;* orcid.org/0000-0002-4661-066X; Email: rvankayala@iitj.ac.in

Authors

Rahul Kumar − *Department of Bioscience and Bioengineering, Indian Institute of Technology Jodhpur, Karwar 342030, India*

Antony Vincy − *Department of Bioscience and Bioengineering, Indian Institute of Technology Jodhpur, Karwar 342030, India*

Khushboo Rani − *Department of Bioscience and Bioengineering, Indian Institute of Technology Jodhpur, Karwar 342030, India*

Neha Jain − *Department of Bioscience and Bioengineering, Indian Institute of Technology Jodhpur, Karwar 342030, India; Centre for Emerging Technologies for Sustainable Development (CETSD), Indian Institute of Technology Jodhpur, Karwar 342030, India;* orcid.org/0000-0001-6269-5619

Sarvar Singh − *Department of Electrical Engineering, Indian Institute of Technology Jodhpur, Karwar 342030, India*

Ajay Agarwal − *Interdisciplinary Research Platform Smart Healthcare and Department of Electrical Engineering, Indian Institute of Technology Jodhpur, Karwar 342030, India*

Complete contact information is available at: https://pubs.acs.org/10.1021/acsomega.3c05485

Author Contributions

R.K., A.V., and K.R., performed the experiments, analyzed the data, and drafted the manuscript. R.V. and N.J. conceptualized the work, designed the experiments, and prepared the final version of the manuscript. S.S. and A.A. helped with the Raman spectroscopy characterization. All authors have read and agreed to the published version of the manuscript.

Funding

R.V. acknowledges the funding support provided by the Department of Biotechnology (DBT), Government of India for the Ramalingaswami Biomedical Fellowship (BT/RLF/Re-entry/17/2018), the seed grant (I/SEED/RRV/20200076) funded by IIT Jodhpur, and Jodhpur City Knowledge and Innovation Cluster, IIT Jodhpur (JCKIF/Thar/Proj-01/2022). N.J. acknowledges the seed grant (I/Seed/NJ/20190019) from the Indian Institute of Technology, Jodhpur and the Early Career Research Award (ECR/2018/002490) from the Science and Engineering Research Board, Department of Science and Technology, Government of India.

Notes

The authors declare no competing financial interest.

■ ACKNOWLEDGMENTS

The authors acknowledge Professor Surajit Ghosh from the Department of Bioscience and Bioengineering, Indian Institute of Technology, Jodhpur, for lending the fluorimeter facilities to

carry out the experiments. The authors acknowledge the FE-SEM facility at the Centre for Research and Development of Scientific Instruments (CRDSI) Facility at the Indian Institute of Technology, Jodhpur.

REFERENCES

(1) Khan, I.; Saeed, K.; Khan, I. Nanoparticles: Properties, Applications and Toxicities. *Arabian J. Chem.* **2019**, *12*, 908−931.
(2) Jeevanandam, J.; Barhoum, A.; Chan, Y. S.; Dufresne, A.; Danquah, M. K. Review on Nanoparticles and Nanostructured Materials: History, Sources, Toxicity and Regulations. *Beilstein J. Nanotechnol.* **2018**, *9*, 1050−1074.
(3) Patil, S.; Chandrasekaran, R. Biogenic Nanoparticles: A Comprehensive Perspective in Synthesis, Characterization, Application and Its Challenges. *J. Genet. Eng. Biotechnol.* **2020**, *18*, No. 67.
(4) Bhardwaj, B.; Singh, P.; Kumar, A.; Kumar, S.; Budhwar, V. Eco-Friendly Greener Synthesis of Nanoparticles. *Adv. Pharm. Bull.* **2020**, *10*, 566−576.
(5) Chae, A.; Choi, B. R.; Choi, Y.; Jo, S.; Kang, E. B.; Lee, H.; Park, S. Y.; In, I. Mechanochemical Synthesis of Fluorescent Carbon Dots from Cellulose Powders. *Nanotechnology* **2018**, *29* (16), No. 165604, DOI: 10.1088/1361-6528/aaad49.
(6) Du, F.; Zhang, M.; Li, X.; Li, J.; Jiang, X.; Li, Z.; Hua, Y.; Shao, G.; Jin, J.; Shao, Q.; Zhou, M.; Gong, A. Economical and Green Synthesis of Bagasse-Derived Fluorescent Carbon Dots for Biomedical Applications. *Nanotechnology* **2014**, *25* (31), No. 315702, DOI: 10.1088/0957-4484/25/31/315702.
(7) Das, P.; Bose, M.; Ganguly, S.; Mondal, S.; Das, A. K.; Banerjee, S.; Das, N. C. Green Approach to Photoluminescent Carbon Dots for Imaging of Gram-Negative Bacteria *Escherichia Coli*. *Nanotechnology* **2017**, *28* (19), No. 195501, DOI: 10.1088/1361-6528/aa6714.
(8) Lee, H.; Padhi, E.; Hasegawa, Y.; Larke, J.; Parenti, M.; Wang, A.; Hernell, O.; Lönnerdal, B.; Slupsky, C. Compositional Dynamics of the Milk Fat Globule and Its Role in Infant Development. *Front. Pediatr.* **2018**, *6* (13), No. 313, DOI: 10.3389/fped.2018.00313.
(9) Bakry, I. A.; Yang, L.; Farag, M. A.; Korma, S. A.; Khalifa, I.; Cacciotti, I.; Ziedan, N. I.; Jin, J.; Jin, Q.; Wei, W.; Wang, X. A Comprehensive Review of the Composition, Nutritional Value, and Functional Properties of Camel Milk Fat. *Foods* **2021**, *10* (9), No. 2158, DOI: 10.3390/foods10092158.
(10) Kula, J. Medicinal Values of Camel Milk. *Int. J. Vet. Sci.* **2016**, *2* (1), 018−025.
(11) Swelum, A. A.; El-Saadony, M. T.; Abdo, M.; Ombarak, R. A.; Hussein, E. O. S.; Suliman, G.; Alhimaidi, A. R.; Ammari, A. A.; Ba-Awadh, H.; Taha, A. E.; El-Tarabily, K. A.; Abd El-Hack, M. E. Nutritional, Antimicrobial and Medicinal Properties of Camel's Milk: A Review. *Saudi J. Biol. Sci.* **2021**, *28*, 3126−3136.
(12) Seifu, E. Recent Advances on Camel Milk: Nutritional and Health Benefits and Processing Implications—A Review. *AIMS Agric. Food* **2022**, *7* (4), 777−804.
(13) Yaseen, G.; Al-Dmoor, H. M. Miraculous Properties of Camel Milk and Perspective of Modern Science. *J. Fam Med. Dis Prev* **2019**, *5* (1), No. 095, DOI: 10.23937/2469-5793/1510095.
(14) Al Nohair, S. F. Medical Benefits of Camel's Milk: A Comprehensive Review. *J. Pak Med. Assoc.* **2021**, *71*, 933−937, DOI: 10.47391/JPMA.367.
(15) Al-Numair, N. S.; Theyab, A.; Alzahrani, F.; Shams, A. M.; Al-Anazi, I. O.; Oyouni, A. A. A.; Al-Amer, O. M.; Mavromatis, C.; Saadeldin, I. M.; Abdali, W. A.; Hawsawi, Y. M. Camels' Biological Fluids Contained Nanobodies: Promising Avenue in Cancer Therapy. *Cancer Cell Int.* **2022**, *22* (1), No. 297, DOI: 10.1186/s12935-022-02696-7.
(16) Krishnankutty, R.; Iskandarani, A.; Therachiyil, L.; Uddin, S.; Azizi, F.; Kulinski, M.; Bhat, A. A.; Mohammad, R. M. Anticancer Activity of Camel Milk via Induction of Autophagic Death in Human Colorectal and Breast Cancer Cells. *Asian Pac. J. Cancer Prev.* **2018**, *19* (12), 3501−3509.
(17) Mirmiran, P.; Ejtahed, H. S.; Angoorani, P.; Eslami, F.; Azizi, F. Camel Milk Has Beneficial Effects on Diabetes Mellitus: A Systematic Review. *Int. J. Endocrinol. Metab.* **2017**, *15*, No. 42150.
(18) Wan, J.; Zhang, X.; Fu, K.; Zhang, X.; Shang, L.; Su, Z. Highly Fluorescent Carbon Dots as Novel Theranostic Agents for Biomedical Applications. *Nanoscale* **2021**, *13*, 17236−17253.
(19) Cui, L.; Ren, X.; Sun, M.; Liu, H.; Xia, L. Carbon Dots: Synthesis, Properties and Applications. *Nanomater* **2021**, *11*, No. 3419.
(20) Chahal, S.; Macairan, J. R.; Yousefi, N.; Tufenkji, N.; Naccache, R. Green Synthesis of Carbon Dots and Their Applications. *RSC Adv.* **2021**, *11*, 25354−25363.
(21) Raveendran, V.; Kizhakayil, R. N. Fluorescent Carbon Dots as Biosensor, Green Reductant, and Biomarker. *ACS Omega* **2021**, *6* (36), 23475−23484.
(22) Liu, J.; Li, R.; Yang, B. Carbon Dots: A New Type of Carbon-Based Nanomaterial with Wide Applications. *ACS Cent. Sci.* **2020**, *6* (12), 2179−2195.
(23) Athika, M.; Prasath, A.; Duraisamy, E.; Sankar Devi, V.; Selva Sharma, A.; Elumalai, P. Carbon-Quantum Dots Derived from Denatured Milk for Efficient Chromium-Ion Sensing and Supercapacitor Applications. *Mater. Lett.* **2019**, *241*, 156−159.
(24) Li, M.; Chen, T.; Gooding, J. J.; Liu, J. Review of Carbon and Graphene Quantum Dots for Sensing. *ACS Sens* **2019**, *4* (7), 1732−1748.
(25) Yoo, D.; Park, Y.; Cheon, B.; Park, M. H. Carbon Dots as an Effective Fluorescent Sensing Platform for Metal Ion Detection. *Nanoscale Res. Lett.* **2019**, *14*, No. 272.
(26) Chaudhary, S.; Kumar, S.; Kaur, B.; Mehta, S. K. Potential Prospects for Carbon Dots as a Fluorescence Sensing Probe for Metal Ions. *RSC Adv.* **2016**, *6* (93), 90526−90536.
(27) An, J.; Liu, G.; Chen, M.; Hu, Y.; Chen, R.; Lyu, Y.; Zhang, C.; Liu, Y. One-Step Synthesis of Fluorescence-Enhanced Carbon Dots for Fe (III) on-off-on Sensing, Bioimaging and Light-Emitting Devices. *Nanotechnology* **2021**, *32* (28), No. 285501, DOI: 10.1088/1361-6528/abf59b.
(28) Lisa John, V.; P M, F.; K P, C.; T P, V. Carbon Dots Derived from Frankincense Soot for Ratiometric and Colorimetric Detection of Lead (II). *Nanotechnology* **2022**, *33* (49), No. 495706, DOI: 10.1088/1361-6528/ac8e76.
(29) Tchounwou, P. B.; Yedjou, C. G.; Patlolla, A. K.; Sutton, D. J. Heavy Metal Toxicity and the Environment. *Exper. Suppl.* **2012**, *101*, 133−164.
(30) Bharti, P. K.; Kumar, P.; Singh, V. Impact of Industrial Effluents on Ground Water and Soil Quality in the Vicinity of Industrial Area of Panipat City, India. *J. Appl. Nat. Sci.* **2013**, *5* (1), 132−136.
(31) Li, L.; Yang, X. The Essential Element Manganese, Oxidative Stress, and Metabolic Diseases: Links and Interactions. *Oxid. Med. Cell. Longev.* **2018**, *2018*, No. 7580707.
(32) Bowman, A. B.; Kwakye, G. F.; Hernández, E. H.; Aschner, M. Role of Manganese in Neurodegenerative Diseases. *J. Trace Elem. Med. Biol.* **2011**, *25*, 191−203.
(33) Chen, P.; Parmalee, N.; Aschner, M. Genetic Factors and Manganese-Induced Neurotoxicity. *Front. Genet.* **2014**, *5*, No. 265.
(34) Harischandra, D. S.; Ghaisas, S.; Zenitsky, G.; Jin, H.; Kanthasamy, A.; Anantharam, V.; Kanthasamy, A. G. Manganese-Induced Neurotoxicity: New Insights into the Triad of Protein Misfolding, Mitochondrial Impairment, and Neuroinflammation. *Front. Neurosci.* **2019**, *13* (5), No. 654, DOI: 10.3389/fnins.2019.00654.
(35) Xu, B.; Huang, S.; Liu, Y.; Wan, C.; Gu, Y.; Wang, D.; Yu, H. Manganese Promotes α-Synuclein Amyloid Aggregation through the Induction of Protein Phase Transition. *J. Biol. Chem.* **2022**, *298* (1), No. 101469, DOI: 10.1016/j.jbc.2021.101469.
(36) Serratos, I. N.; Hernández-Pérez, E.; Campos, C.; Aschner, M.; Santamaría, A. An Update on the Critical Role of α-Synuclein in Parkinson's Disease and Other Synucleinopathies: From Tissue to Cellular and Molecular Levels. *Mol. Neurobiol.* **2022**, *59*, 620−642.

https://doi.org/10.1021/acsomega.3c05485
ACS Omega 2023, 8, 36521−36533

(37) Yang, W.; Hamilton, J. L.; Kopil, C.; Beck, J. C.; Tanner, C. M.; Albin, R. L.; Ray Dorsey, E.; Dahodwala, N.; Cintina, I.; Hogan, P.; Thompson, T. Current and Projected Future Economic Burden of Parkinson's Disease in the U.S. *npj Parkinson's Dis.* **2020**, *6* (1), No. 15, DOI: 10.1038/s41531-020-0117-1.
(38) Tsoi, P. S.; Quan, M. D.; Ferreon, J. C.; Ferreon, A. C. M. Aggregation of Disordered Proteins Associated with Neurodegeneration. *Int. J. Mol. Sci.* **2023**, *24*, 3380.
(39) Yang, Y.; Shi, Y.; Schweighauser, M.; Zhang, X.; Kotecha, A.; Murzin, A. G.; Garringer, H. J.; Cullinane, P. W.; Saito, Y.; Foroud, T.; Warner, T. T.; Hasegawa, K.; Vidal, R.; Murayama, S.; Revesz, T.; Ghetti, B.; Hasegawa, M.; Lashley, T.; Scheres, S. H. W.; Goedert, M. Structures of α-Synuclein Filaments from Human Brains with Lewy Pathology. *Nature* **2022**, *610* (7933), 791−795.
(40) Burré, J.; Sharma, M.; Tsetsenis, T.; Buchman, V.; Etherton, M. R.; Südhof, T. C. α-Synuclein Promotes SNARE-Complex Assembly in Vivo and in Vitro. *Science* **2010**, *24*, 1663−1667.
(41) Cabin, D. E.; Shimazu, K.; Murphy, D.; Cole, N. B.; Gottschalk, W.; Mcilwain, K. L.; Orrison, B.; Chen, A.; Ellis, C. E.; Paylor, R.; Lu, B.; Nussbaum, R. L. Synaptic Vesicle Depletion Correlates with Attenuated Synaptic Responses to Prolonged Repetitive Stimulation in Mice Lacking-Synuclein. *J. Neurosci.* **2002**, *22* (20), 8797−8807.
(42) Nguyen, P. H.; Ramamoorthy, A.; Sahoo, B. R.; Zheng, J.; Faller, P.; Straub, J. E.; Dominguez, L.; Shea, J. E.; Dokholyan, N. V.; de Simone, A.; Ma, B.; Nussinov, R.; Najafi, S.; Ngo, S. T.; Loquet, A.; Chiricotto, M.; Ganguly, P.; McCarty, J.; Li, M. S.; Hall, C.; Wang, Y.; Miller, Y.; Melchionna, S.; Habenstein, B.; Timr, S.; Chen, J.; Hnath, B.; Strodel, B.; Kayed, R.; Lesné, S.; Wei, G.; Sterpone, F.; Doig, A. J.; Derreumaux, P. Amyloid Oligomers: A Joint Experimental/Computational Perspective on Alzheimer's Disease, Parkinson's Disease, Type II Diabetes, and Amyotrophic Lateral Sclerosis. *Chem. Rev.* **2021**, *121*, 2545−2647.
(43) Jomova, K.; Makova, M.; Alomar, S. Y.; Alwasel, S. H.; Nepovimova, E.; Kuca, K.; Rhodes, C. J.; Valko, M. Essential Metals in Health and Disease. *Chem.-Biol. Interact.* **2022**, *367*, No. 110173.
(44) Hu, Q.; Liu, L. F.; Sun, H.; Han, J.; Gong, X.; Liu, L.; Yang, Z. Q. An Ultra-Selective Fluorescence Method with Enhanced Sensitivity for the Determination of Manganese (VII) in Food Stuffs Using Carbon Quantum Dots as Nanoprobe. *J. Food Compos. Anal.* **2020**, *88*, No. 103447, DOI: 10.1016/j.jfca.2020.103447.
(45) Liang, P.; Sun, Z.; Cao, J. Speciation of Mn(II) and Mn(VII) in Water Samples by Cloud Point Extraction Separation and Their Determination by Graphite Furnace Atomic Absorption Spectrometry. *At. Spectrosc.* **2007**, *28*, 62.
(46) Batool, M.; Junaid, H. M.; Tabassum, S.; Kanwal, F.; Abid, K.; Fatima, Z.; Shah, A. T. Metal Ion Detection by Carbon Dots—A Review. *Crit. Rev. Anal. Chem.* **2022**, *52*, 756−767.
(47) Yoo, D.; Park, Y.; Cheon, B.; Park, M. H. Carbon Dots as an Effective Fluorescent Sensing Platform for Metal Ion Detection. *Nanoscale Res. Lett.* **2019**, *14*, No. 272.
(48) Gao, X.; Du, C.; Zhuang, Z.; Chen, W. Carbon Quantum Dot-Based Nanoprobes for Metal Ion Detection. *J. Mater. Chem. C* **2016**, *4*, 6927−6945.
(49) Du, F.; Li, G.; Gong, X.; Zhonghui, G.; Shuang, S.; Xian, M.; Dong, C. Facile, Rapid Synthesis of N,P-Dual-Doped Carbon Dots as a Label-Free Multifunctional Nanosensor for Mn(VII) Detection, Temperature Sensing and Cellular Imaging. *Sens Actuators, B* **2018**, *277*, 492−501.
(50) Deng, P.; Lu, L. Q.; Cao, W. C.; Tian, X. K. Phosphorescence Detection of Manganese(VII) Based on Mn-Doped ZnS Quantum Dots. *Spectrochim. Acta, Part A* **2017**, *173*, 578−583.
(51) Mohammed, A.; Gugulothu, Y.; Bandi, R.; Dadigala, R.; Utkoor, U. K. Ultraspeed Synthesis of Highly Fluorescent N-Doped Carbon Dots for the Label-Free Detection of Manganese (VII). *J. Chin. Chem. Soc.* **2021**, *68* (8), 1514−1521.
(52) Mohagheghpour, E.; Farzin, L.; Ghoorchian, A.; Sadjadi, S.; Abdouss, M. Selective Detection of Manganese(II) Ions Based on the Fluorescence Turn-on Response via Histidine Functionalized Carbon Quantum Dots. *Spectrochim. Acta, Part A* **2022**, *279*. DOI: 10.1016/j.saa.2022.121409.
(53) Zhang, X.; Ren, G.; He, Z.; Yang, W.; Li, H.; Wang, Y.; Pan, Q.; Shi, X. Luminescent Detection of Cr(VI) and Mn(VII) Based on a Stable Supramolecular Organic Framework. *Cryst. Growth Des.* **2020**, *20* (10), 6888−6895.
(54) Wang, L.; Zhou, H. S. Green Synthesis of Luminescent Nitrogen-Doped Carbon Dots from Milk and Its Imaging Application. *Anal. Chem.* **2014**, *86* (18), 8902−8905.
(55) Jain, N.; Bhasne, K.; Hemaswasthi, M.; Mukhopadhyay, S. Structural and Dynamical Insights into the Membrane-Bound α-Synuclein. *PLoS One* **2013**, *8* (12), No. e83752, DOI: 10.1371/journal.pone.0083752.
(56) Sharma, S. K.; Chorell, E.; Steneberg, P.; Vernersson-Lindahl, E.; Edlund, H.; Wittung-Stafshede, P. Insulin-Degrading Enzyme Prevents α-Synuclein Fibril Formation in a Nonproteolytical Manner. *Sci. Rep.* **2015**, *5*, No. 12531, DOI: 10.1038/srep12531.
(57) Ban, D. K.; Paul, S. Nano Zinc Oxide Inhibits Fibrillar Growth and Suppresses Cellular Toxicity of Lysozyme Amyloid. *ACS Appl. Mater. Interfaces* **2016**, *8* (46), 31587−31601.
(58) Kim, T. D.; Paik, S. R.; Yang, C. H. Structural and Functional Implications of C-Terminal Regions of α-Synuclein. *Biochemistry* **2002**, *41* (46), 13782−13790.
(59) Liu, X.; Huang, H.; Liu, G.; Zhou, W.; Chen, Y.; Jin, Q.; Ji, J. Multidentate Zwitterionic Chitosan Oligosaccharide Modified Gold Nanoparticles: Stability, Biocompatibility and Cell Interactions. *Nanoscale* **2013**, *5* (9), 3982−3991.
(60) Sahu, S.; Behera, B.; Maiti, T. K.; Mohapatra, S. Simple One-Step Synthesis of Highly Luminescent Carbon Dots from Orange Juice: Application as Excellent Bio-Imaging Agents. *ChemComm* **2012**, *48* (70), 8835−8837.
(61) Danaei, M.; Dehghankhold, M.; Ataei, S.; Hasanzadeh Davarani, F.; Javanmard, R.; Dokhani, A.; Khorasani, S.; Mozafari, M. R. Impact of Particle Size and Polydispersity Index on the Clinical Applications of Lipidic Nanocarrier Systems. *Pharmaceutics* **2018**, *10* (5), No. 57, DOI: 10.3390/pharmaceutics10020057.
(62) Vinci, J. C.; Ferrer, I. M.; Guterry, N. W.; Colón, V. M.; Destino, J. F.; Bright, F. V.; Colón, L. A. Spectroscopic Characteristics of Carbon Dots (C-Dots) Derived from Carbon Fibers and Conversion to Sulfur-Bridged C-Dots Nanosheets. *Appl. Spectrosc.* **2015**, *69* (9), 1082−1090.
(63) Tepliakov, N. V.; Kundelev, E. V.; Khavlyuk, P. D.; Xiong, Y.; Leonov, M. Y.; Zhu, W.; Baranov, A. V.; Fedorov, A. V.; Rogach, A. L.; Rukhlenko, I. D. Sp2-Sp3-Hybridized Atomic Domains Determine Optical Features of Carbon Dots. *ACS Nano* **2019**, *13* (9), 10737−10744.
(64) Choi, Y.; Thongsai, N.; Chae, A.; Jo, S.; Kang, E. B.; Paoprasert, P.; Park, S. Y.; In, I. Microwave-Assisted Synthesis of Luminescent and Biocompatible Lysine-Based Carbon Quantum Dots. *J. Ind. Eng. Chem.* **2017**, *47*, 329−335.
(65) Zhang, L.; Li, B.; Zhou, Y.; Wu, Y.; Le, T.; Sun, Q. Green Synthesis of Cow Milk-Derived Carbon Quantum Dots and Application for Fe^{3+} Detection. *J. Solgel Sci. Technol.* **2023**, *106*, 173−185.
(66) Kumar, A.; Kumar, I.; Gathania, A. K. Synthesis, Characterization and Potential Sensing Application of Carbon Dots Synthesized via the Hydrothermal Treatment of Cow Milk. *Sci. Rep* **2022**, *12* (1), No. 22495, DOI: 10.1038/s41598-022-26906-4.
(67) Murugan, N.; Sundramoorthy, A. K. Green Synthesis of Fluorescent Carbon Dots from Borassus Flabellifer Flowers for Label-Free Highly Selective and Sensitive Detection of Fe^{3+} Ions. *New J. Chem.* **2018**, *42* (16), 13297−13307.
(68) Ding, H.; Li, X. H.; Chen, X. B.; Wei, J. S.; Li, X. B.; Xiong, H. M. Surface States of Carbon Dots and Their Influences on Luminescence. *J. Appl. Phys.* **2020**, *127* (23), No. 231101, DOI: 10.1063/1.5143819.
(69) Gan, Z.; Xu, H.; Hao, Y. Mechanism for Excitation-Dependent Photoluminescence from Graphene Quantum Dots and Other

https://doi.org/10.1021/acsomega.3c05485
ACS Omega 2023, 8, 36521−36533

Graphene Oxide Derivates: Consensus, Debates and Challenges. *Nanoscale* **2016**, *8*, 7794−7807.
(70) Balakrishnan, T.; Ang, W. L.; Mahmoudi, E.; Mohammad, A. W.; Sambudi, N. S. Formation Mechanism and Application Potential of Carbon Dots Synthesized from Palm Kernel Shell via Microwave Assisted Method. *Carbon Resour. Convers.* **2022**, *5* (2), 150−166.
(71) Lin, H.; Huang, J.; Ding, L. Preparation of Carbon Dots with High-Fluorescence Quantum Yield and Their Application in Dopamine Fluorescence Probe and Cellular Imaging. *J. Nanomater.* **2019**, *2019*, No. 5037243, DOI: 10.1155/2019/5037243.
(72) Shrivastava, A.; Gupta, V. Methods for the Determination of Limit of Detection and Limit of Quantitation of the Analytical Methods. *Chron. Young Sci.* **2011**, *2* (1), 21.
(73) Laptinskiy, K. A.; Burikov, S. A.; Chugreeva, G. N.; Dolenko, T. A. The Mechanisms of Fluorescence Quenching of Carbon Dots upon Interaction with Heavy Metal Cations. *Fullerenes, Nanotubes Carbon Nanostruct.* **2022**, *30* (1), 46−52.
(74) Smrithi, S. P.; Kottam, N.; Muktha, H.; Mahule, A. M.; Chamarti, K.; Vismaya, V.; Sharath, R. Carbon Dots Derived from Beta Vulgaris: Evaluation of Its Potential as Antioxidant and Anticancer Agent. *Nanotechnol.* **2022**, *33* (4), No. 045403, DOI: 10.1088/1361-6528/ac30f1.
(75) Xue, C.; Lin, T. Y.; Chang, D.; Guo, Z. Thioflavin T as an Amyloid Dye: Fibril Quantification, Optimal Concentration and Effect on Aggregation. *R. Soc. Open Sci.* **2017**, *4* (1), No. 160696, DOI: 10.1098/rsos.160696.

https://doi.org/10.1021/acsomega.3c05485
ACS Omega 2023, 8, 36521−36533